

Revealing the microstructures of metal halide perovskite thin films via advanced transmission electron microscopy

Yeming Xian(冼业铭), Xiaoming Wang(王晓明), and Yanfa Yan(鄢炎发)

Citation: Chin. Phys. B, 2024, 33 (**9**): 096803. DOI: 10.1088/1674-1056/ad6259
Journal homepage: http://cpb.iphy.ac.cn; http://iopscience.iop.org/cpb

What follows is a list of articles you may be interested in

Symmetry quantification and segmentation in STEM imaging through Zernike moments

Jiadong Dan, Cheng Zhang, Xiaoxu Zhao(赵晓续), and N. Duane Loh
Chin. Phys. B, 2024, 33 (**8**): 086803. DOI: 10.1088/1674-1056/ad51f4

Anomalous strain effect in heteroepitaxial $SrRuO_3$ films on (111) $SrTiO_3$ substrates

Zhenzhen Wang(王珍珍), Weiheng Qi(戚炜恒), Jiachang Bi(毕佳畅), Xinyan Li(李欣岩), Yu Chen(陈雨), Fang Yang(杨芳), Yanwei Cao(曹彦伟), Lin Gu(谷林), Qinghua Zhang(张庆华), Huanhua Wang(王焕华), Jiandi Zhang(张坚地), Jiandong Guo(郭建东), and Xiaoran Liu(刘笑然)
Chin. Phys. B, 2022, 31 (**12**): 126801. DOI: 10.1088/1674-1056/ac8725

In-plane oriented $CH_3NH_3PbI_3$ nanowire suppression of the interface electron transfer to PCBM

Tao Wang(王涛), Zhao-Hui Yu(于朝辉), Hao Huang(黄昊), Wei-Guang Kong(孔伟光), Wei Dang(党伟), and Xiao-Hui Zhao(赵晓辉)
Chin. Phys. B, 2021, 30 (**6**): 066801. DOI: 10.1088/1674-1056/abf4fa

O_3 fast and simple treatment-enhanced p-doped in Spiro-MeOTAD for CH_3NH_3I vapor-assisted processed $CH_3NH_3PbI_3$ perovskite solar cells

En-Dong Jia(贾恩东), Xi Lou(娄茜), Chun-Lan Zhou(周春兰), Wei-Chang Hao(郝维昌), Wen-Jing Wang(王文静)
Chin. Phys. B, 2017, 26 (**6**): 068803. DOI: 10.1088/1674-1056/26/6/068803

Aberration-corrected scanning transmission electron microscopy for complex transition metal oxides

Qing-Hua Zhang(张庆华), Dong-Dong Xiao(肖东东), Lin Gu(谷林)
Chin. Phys. B, 2016, 25 (**6**): 066803. DOI: 10.1088/1674-1056/25/6/066803

TOPICAL REVIEW — Stephen J. Pennycook: A research life in atomic-resolution STEM and EELS

Revealing the microstructures of metal halide perovskite thin films via advanced transmission electron microscopy

Yeming Xian(冼业铭), Xiaoming Wang(王晓明), and Yanfa Yan(鄢炎发)[†]

Department of Physics and Astronomy and Wright Center for Photovoltaics Innovation and Commercialization, The University of Toledo, Toledo, Ohio 43606, *United States*

(Received 3 April 2024; revised manuscript received 15 May 2024; accepted manuscript online 12 July 2024)

Metal halide perovskites (MHPs) are excellent semiconductors that have led to breakthroughs in applications in thin-film solar cells, detectors, and light-emitting diodes due to their remarkable optoelectronic properties and defect tolerance. However, the performance and stability of MHP-based devices are significantly influenced by their microstructures including the formation of defects, composition fluctuations, structural inhomogeneity, etc. Transmission electron microscopy (TEM) is a powerful tool for direct observation of microstructure at the atomic-scale resolution and has been used to correlate the microstructure and performance of MHP-based devices. In this review, we highlight the application of TEM techniques in revealing the microstructures of MHP thin films at the atomic scale. The results provide critical understanding of the performance of MHP devices and guide the design of strategies for improving the performance and stability of MHP devices.

Keywords: perovskite, defect, inhomogeneity, transmission electron microscopy

PACS: 68.35.Dv, 68.37.Lp, 68.37.Ma, 68.37.Og **DOI:** 10.1088/1674-1056/ad6259

1. Introduction

Metal halide perovskites (MHPs) have emerged as promising materials for various optoelectronic applications, including photovoltaics,[1–3] light-emitting diodes,[4–6] and photodetectors,[7–9] owing to their remarkable optoelectronic properties and simple synthesized process. The performance and stability of MHP devices critically depend on the structure of MHP thin films, including composition fluctuation,[10,11] defects,[12] grain boundaries,[13,14] phase segregation,[15,16] etc., which introduce unique microstructural inhomogeneity that breaks the uniform atomic distribution. Such microstructural inhomogeneity needs to be carefully studied in terms of the origins of formation and how it influences the electronic and optoelectronic properties of MHPs. Revealing the microstructural inhomogeneity of MHP thin films and correlating them with the performance of MHP devices provide critical information for developing strategies to further improve the performance and stability of MHP devices.[17–20]

Transmission electron microscopy (TEM) and scanning transmission electron microscopy (STEM) have emerged as indispensable tools in materials science, providing unparalleled insights into the microstructure of thin films at the nanoscale, which is crucial for elucidating the electronic properties of the studied materials.[21–23] TEM has been extensively used to reveal the microstructures of MHP thin films. Despite the growing interest in perovskite-based technologies, no comprehensive review focused on the application of TEM in studying the microstructure of perovskite thin films. Thus, this review aims to fill this gap by providing a comprehensive overview of the advancements in utilizing TEM for the characterization of the microstructure of MHP thin films.

Here, we summarize the utilization of TEM and STEM imaging for direct observation of microstructural inhomogeneity of MHP thin films. The observation allowed the understanding of the formation of defects, both in intragrain regions and at the surface/interface regions, phase inhomogeneity, and degradation. The defects could be either intrinsic or originated from structural degradation.

2. Transmission electron microscopy – basic and extended methods and applications in MHPs

MHP materials exhibit greater heterogeneity and possess a more intricate and imperfect structure when compared to conventional photovoltaic materials like silicon and cadmium telluride (CdTe). They often incorporate nanoparticles and exhibit various defects or nanoscale structuring, all of which significantly influence their physical properties and device performance. Given their complexity, TEM techniques are well-matched for investigating these materials, offering diverse imaging modes and analytical capabilities. In this section, we summarize the basic methods of transmission electron microscopy used in previous researches for direct acquisition of lattice- and atomic-resolved information in MHPs, as shown in Table 1. Such advanced TEM techniques have enabled direct and precise observations of microstructural inhomogeneity of MHPs at lattice and atomic levels, which are discussed in the following sections.

[†]Corresponding author. E-mail: yanfa.yan@utoledo.edu

© 2024 Chinese Physical Society and IOP Publishing Ltd

Table 1. Summary of basic and extended applications of TEM and STEM techniques along with corresponding halide perovskite specimens as reported in previous researches.

TEM technique	Perovskite (specimen morphology)	Brief description of application
SAED	$MAPbI_3$ (microplate,[24] nanonet[25])	Selected area electron diffraction, SAED patterns can be employed to determine crystal orientation, lattice constants, or examine its defects.
HRTEM	$MAPbI_3$ (particle),[26] $MAPbBr_3$ (nanocrystal),[27] $MAPb(I_{0.6}Br_{0.4})_3$ (film),[28] $CsPbBr_3$ (nanosheet),[29] $(2T)_2PbI_4$ (single crystal),[30] $(2T)_2PbBr_4$ (single crystal)[30]	High-resolution transmission electron microscopy, an imaging mode of the TEM enabling visualization of the atomic-scale crystallographic structure of a sample.
CTF-corrected HRTEM	$MAPbBr_3$ (nanocrystal)[27]	Correction for contrast transfer function is essential to extract high-resolution details from TEM images affected by imperfect imaging conditions, thereby enabling the creation of an accurate representation of the specimen at high resolution.
In situ TEM	$MAPbI_3$ (film)[31]	*In situ* transmission electron microscopy offers real-time observations of material behavior as it responds to various external stimuli like temperature changes, alterations in gas environment, applied stress, and electric or magnetic fields.
Cryo-TEM	$MAPbI_3$ (particle, nanowire),[26,32] $MAPbBr_3$ (nanowire)[32]	Transmission electron cryomicroscopy is subtype of transmission electron microscopy that involves studying samples at cryogenic temperatures.
HAADF-STEM	$CsPbBr_3$ (nanocrystal, nanowire),[33,34] $CsPbI_3$ (nanocrystal, nanorod),[33,34] $(RNH_3)_2(A)_{n-1}B_nX_{3n+1}$ (nanosheet)[15]	High-angle annular dark-field imaging, a technique in STEM, is utilized to pinpoint regions containing elements with high atomic numbers (Z) within a matrix of materials possessing lower Z, particularly in heterogeneous materials, owing to its significant reliance on atomic number Z.
LAADF-STEM	$FAPbI_3$ (film)[12]	Low-angle annular dark-field STEM serves as a substitute for HAADF-STEM when examining specimens composed solely of light elements.
iDPC-STEM	$CsPbI_3$ (nanocrystal, quantum dot)[35,36]	Integrated differential phase contrast STEM enhances the ability to detect light elements amidst heavy elements within a single image, allowing for the imaging of both light and heavy atoms in a thin sample.
STEM-EDX	K^+-doped $Cs_{0.05}(FA_{0.85}MA_{0.15})_{0.95}Pb(I_{0.85}Br_{0.15})_3$ (film),[37] $MAPbI_3$ (film)[38]	Energy-dispersive x-ray spectroscopy in STEM is commonly employed for analyzing composition and mapping elements within samples.
EELS	$MAPbI_3$ (film, quantum dot)[39,40]	Electron energy loss spectroscopy in STEM can be utilized for both spectroscopic chemical mapping and atomic-resolution elemental mapping.

Despite being a powerful tool for studying the structural properties of MHPs at the nanoscale, challenges still remain when it comes to using TEM effectively. A primary challenge is the beam damage, which refers to the structural changes induced by the high-energy electron beam used in TEM imaging. Beam damage can result in distortions in MHP structures, changes in chemical composition and phase transformations, compromising the accuracy and reliability of the obtained results. To mitigate the beam damage of MHPs when utilizing TEM, one can reduce the electron dose which limits the total electron dose received by the sample. Lower beam energies and shorter exposure time also help to minimize beam damage while maintaining sufficient imaging resolution.

3. Intragrain defects and surface/interface defects induced microstructural inhomogeneity

Generally speaking, inhomogeneity in MHPs can be roughly categorized as defect-related and defect-irrelated. In this section, we focus on discussing the direct observation of defect-related homogeneity in MHPs at the atomic level via the transmission electron microscopy, including intragrain point defects, line defects and planar defects, and nanoscale observation of defects on the surface and interfaces of per-

ovskites, as discussed accordingly below.

3.1. Intragrain line defects

Edge dislocations are the mostly observed line defects in MHPs and they exist in both three-dimensional and two-dimensional perovskites. Edge dislocations are present in $FAPbI_3$ perovskite, which are classified as climb-dissociated because the dislocations exhibit dissociation along the direction perpendicular to their glide planes. And a region of PbI_2 that forms planar fault joining the dislocation was also clearly observed.[12] Microstructures of $CsPbBr_3$ films prepared by one-step sintering (OSS) and two-step sintering (TSS) methods were also unveiled by TEM and HRTEM.[41] Inverse FFT analysis along the [111] direction showed large amounts of edge dislocations in the OSS film, while there was no dislocation observed in the TSS at 300 °C film. The observation indicated that the TSS process improved crystallinity and reduced edge dislocations for cubic $CsPbBr_3$ crystals, which led to lower density of line defects and thus enhanced the efficiency of $CsPbBr_3$ optoelectronic devices.

Similar threading dislocations were observed in remote epitaxial $CsPbBr_3$ perovskite via HRTEM.[42] Figure 1(b) shows inverse FFT analysis of its inset with zone axes [11$\bar{2}$], indicating the existence of threading dislocations in remote epitaxial $CsPbBr_3$ samples, which are formed likely due to the large grain coalescence stage. The inset is FFT from HRTEM image of remote epitaxial $CsPbBr_3$/Gr/NaCl ($CsPbBr_3$ flakes grown on monolayer graphene buffered NaCl(001) substrate, Fig. 1(a)). High density of edge dislocations in a local region results in the formation of fringes in perovskites.[43] The TEM imagery, accompanied by SAED patterns of poly(triaryl amine) (PTAA)-based reveals a substantial density of fringes, indicative of an elevated defect density along the [100] zone axis. HRTEM analysis further elucidates that these fringes are constituted by a significant concentration of edge dislocations. This assertion is confirmed by the distinct evidence provided through the application of FFT and its inverse, utilizing the [011] spatial frequencies.

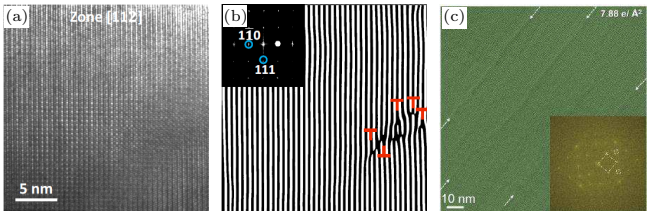


Fig. 1. (a) HRTEM images for remote epitaxial $CsPbBr_3$/Gr/NaCl. (b) Inverse FFT of the inset. The inset is FFT from (a) with additional white spots. Dislocations are indicated by the red "T". (c) HRTEM images showing step edges in a nanoplatelet with an accumulated electron dose of $\sim 7.88\ e{\cdot}Å^{-2}$. Panels (a) and (b) are reproduced with permission from Ref. [42]. Panel (c) is reproduced with permission from Ref. [45].

Despite the negative influence of edge dislocation on charge transport and internal structural stability of MHPs, it helps relax the strain accumulating on the interface and thus stabilizes the interfacial connection of heterostructure. The atomic-scale misfit dislocation of two-dimensional $(2T)_2PbBr_4/(2T)_2PbI_4$ perovskite heterostructure was directly observed by the Fourier filtered AC-HRTEM method.[30,44] The edge dislocations on the interface occur periodically every ~15 nm. Such interfacial mismatch enables the crystal structures to return from the mismatched regions at the interface to the original region in the bulk.

Apart from the atomic-scale line defects in MHPs, larger scale step edges that appear across the length of more than 100 nm were discovered by the HRTEM images.[45] Cryo-HRTEM images demonstrate obvious large-scale step edges in a single-phase $MAPbI_3$ nanoplatelet, and the FFT analysis indicates the tetragonal phase (Fig. 1(c)). It was observed from the magnified view of the step edges that these regions maintain perfect tetragonal phase.

3.2. Intragrain planar defects

Twinning domain is among common planar defects observed at atomic level in MHPs.[46–52] Intragrain twin domain was examined in $FA_{0.5}Cs_{0.5}PbI_3$ perovskite as shown in Fig. 2(a).[49] The FFT pattern derived from the STEM-HAADF image, captured at the twin boundary region, is characterized by two intertwined arrays of distinct patterns, which correspond to an orthorhombic lattice configuration. This analysis showed the intricate atomic configurations of the twin boundary as well as the adjacent MHP lattices. It was observed that the lattice structures flanking the twin boundary exhibited a high degree of symmetry, aligning with the atomic structure model of a $[100]_o$-projected orthorhombic MHP. This finding was in strong concordance with the outcomes derived from the FFT analysis. Intrinsic twin domains were also observed in $MAPbI_3$ perovskite.[51] A bright-field TEM image of a room temperature $MAPbI_3$ thin film is shown in Fig. 2(b), which exhibits strip contrast that consists of parallel bands of alternate dark and bright strip. Further SAED patterns (Fig. 2(c)) for individual $MAPbI_3$ grain show split spots that are related to the twin domains. The SAED pattern consists of two overlapping diffraction patterns of tetragonal $MAPbI_3$ phase with a mirrored reflection relationship, which indicates twin domains. Common diffraction spots from both sides of domains are coincident along the twin axis, while the other diffraction spots from the two domains separate slightly, which is characteristic of twinning.

Another common planar fault observed at atomic scale in MHPs is stacking faults.[12,26,46,47,52–54] High density of $(002)_T$ stacking faults were discovered in $MAPbI_3$ particle via lattice-resolution TEM image and HRTEM image.[26] It is noted that the type of stacking fault in $MAPbI_3$ crystal is related to additional MAI layers along $(002)_T$ surface, which is similar to the inorganic halide perovskite where the dominated type of stacking fault is AX–AX along $(001)_C$ direction with additional AX layers. The stability of stacking faults in

$MAPbI_3$ against beam exposure indicates the intrinsic characteristic of such type of planar defect. Similarly, in another research, high density of stacking faults and twins were found in $MAPbI_3$ grains with negative Cs corrected (NCs-) HRTEM, as shown in Fig. 2(e).[39]

Ruddlesden–Popper (RP) planar faults are a lattice mismatch along the interface between two identical structures on both sides in the same way as the formation of RP perovskite structure.[55,56] A typical RP planar fault was found in $CsPbBr_3$ crystal, where two CsBr layers with rock-salt stacking were sandwiched between two $CsPbBr_3$ domains.[55] The atomic resolution HAADF image of the RP planar fault is shown in Fig. 2(d), which demonstrates rock-salt stacking of CsBr bilayers.

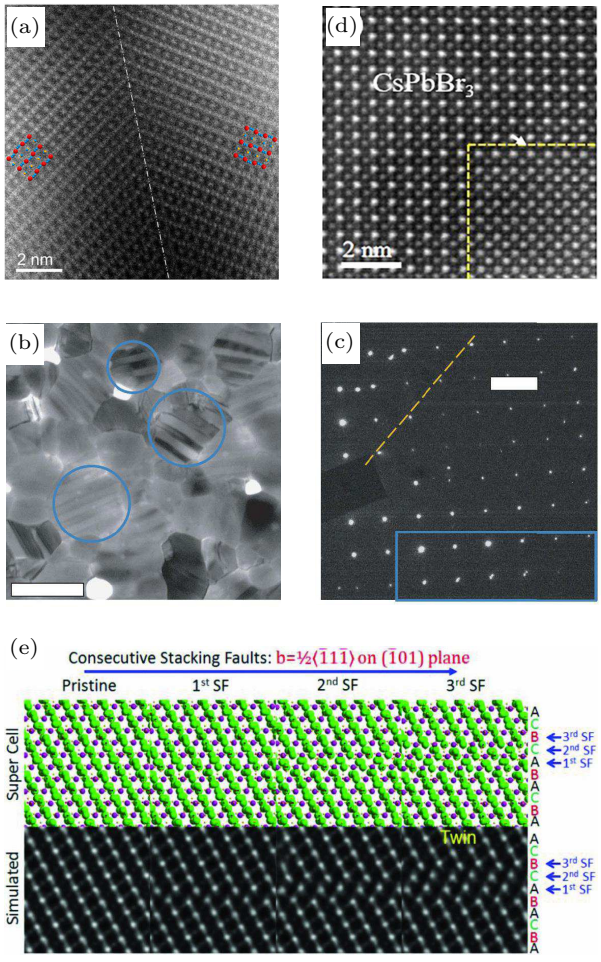


Fig. 2. (a) Atomic-scale Bragg filtered STEM-HAADF image revealing atomic-scale details of the twin boundary in $FA_{0.5}Cs_{0.5}PbI_3$ grains. (b) Bright-field TEM image of the pristine $CH_3NH_3PbI_3$ thin film at room temperature, displaying stripe contrast within some grains (examples circled in blue). (c) Near $[1\bar{1}0]_t$-oriented diffraction pattern captured from a grain with stripe contrast, illustrating two single-crystal patterns with a mirrored relationship. (d) HAADF-STEM image of the detection area encompassing both the matrix (top-left) and nanodomain (bottom-right) regions. (e) A supercell arrangement and simulated HRTEM images below showing the progressive evolution of three stacking faults from left to right, leading to the formation of twins. Panel (a) is reproduced with permission from Ref. [49]. Panels (b) and (c) are reproduced with permission from Ref. [51]. Panel (d) is reproduced with permission from Ref. [55]. Panel (e) is reproduced with permission from Ref. [39].

3.3. Intragrain point defects

As point defects and their effect on charge transport and charge-defect interaction have drawn much research attention, the exact nature of these defects was revealed by Butterworth-filtered atomic-resolution low-angle annular dark field (LAADF) STEM.[12] The presence of aligned vacancy defects on the I/Pb lattice sites in $FAPbI_3$ crystal can be seen. In addition, doping sites originating from external elemental replacement can also be identified by combining the HAADF-STEM and EDS mapping image techniques.[57] The location of Yb^{3+} doping in $CsPbCl_3$:Yb^{3+} perovskite nanocrystals was clearly identified, and its successful substitution for Pb^{2+} lattice sites was further validated by STEM-EDS mapping.

3.4. Surface/interface defects

Surface and interface regions are prone to the formation and retention of defects and traps.[58–62] A virtual bright-field image obtained by PEEM measurements with low-dose scanning electron diffraction (SED) microscopy of a region of $(Cs_{0.05}FA_{0.78}MA_{0.17})Pb(I_{0.83}Br_{0.17})_3$ perovskite thin film was reported by Doherty *et al.*[61] The STEM-EDX map of the bulk parent perovskite region that does not contain trap cluster shows uniform halide distribution. In comparison, an inhomogeneous grain with I aggregation is shown in the STEM-EDX map. The interface of this grain with adjacent pristine perovskite grain exhibits nanoscale trap cluster, and this grain cannot be indexed to a typical cubic perovskite phase by the diffraction pattern.

Surface traps are also common on the surface of perovskite quantum dots (QDs) and can be observed as black spots in the TEM measurements.[60] ZnX_2 treatment facilitates the removal of black spots on the surface of $CsPbX_3$ (X = Cl, Br, I) QDs, which is illustrated by the comparison of TEM images of $CsPbX_3$ QDs before and after ZnX_2 treatment. The disappearance of these black spots enhances the stability of $CsPbX_3$ QDs.

Computational simulation techniques, including structural modeling and density functional theory (DFT) calculations, offer deep insights into the mechanisms linking microstructural features with device performance that are related to electronic structures, defect formation energies and charge transport properties. Zhao *et al.* applied DFT calculations to investigate the defect level via density of states (DOS) of FA and Br vacancies on the $FAPbBr_3$ crystal surface with FABr termination, where a Br vacancy on the surface induces a donor gap state while an FA vacancy on the surface induces an acceptor gap state.[63] Such surface defects act as trap sites for charge carriers, leading to non-radiative recombination and reduced device performance. Different surface/interface engineering strategies have been widely developed and adopted to boost MHP-based device performance.[63–65] Ammonium bromide was introduced as a functional group to passivate the FA vacancies, uncoordinated lead and Pb–Pb

dimers deep traps on $FAPbBr_3$ surface, which enabled near-unity charge collection efficiency in gamma-ray spectrum devices.[63] Chen *et al.* incorporated potassium citrate (PC) into the poly(3,4-ethylenedioxythiophene):poly(styrene sulfonate) (PEDOT:PSS) hole-transport layer to passivate halide defects, prevent Sn^{2+} oxidation and suppress defect formation, which enabled efficient low-bandgap Sn–Pb perovskite solar cells and all-perovskite tandem solar cells.[65] These results emphasize the significance of surface/interface engineering in developing efficient and stable MHP photodetectors and solar cells. Li *et al.* found by DFT calculations that the molecular additive 1,3-bis(diphenylphosphino)propane (DPPP) is more energetically favorable to bind two adjacent perovskite slabs than to bind the same perovskite slab.[66] Likewise, the binding energy for the DPPP to bind both perovskite and NiO_x slabs is larger than to bind the same NiO_x slab. The results indicate that DPPP is able to bind, bridge, and stabilize perovskite GBs and the perovskite/NiO_x interface, which provides charge transport channel for charge extraction, minimizes recombination loss and thus facilitates device efficiency.

4. Multidimensional, grain and phase segregation induced microstructural inhomogeneity

Not all structural inhomogeneities in MHPs are associated with defect formations. Some are introduced intentionally to boost the optoelectrical performance of MHP-based devices, such as multidimensional perovskite solar cells and molecular additives between grain boundaries, while the others occur intrinsically, such as phase segregation. The observation of this non defect-related inhomogeneity in MHPs is demonstrated and discussed in this section, with TEM images playing a critical role.

4.1. Multidimensional distribution

Massive reports about multidimensional perovskite solar cells including 2D–3D, 1D–3D and 1D–2D–3D solar cells utilized TEM and HRTEM measurements to demonstrate the lattice alignment of these heterostructures.[67–77] As Fig. 3(a) shows, fingerprint inter-planar spacing of 3.2 Å was observed in HRTEM images, characteristic of 3D perovskite.[69] The inter-planar spacings of 6.7 Å and 7.1 Å were observed in nearby regions, corresponding to (080) ($n = 3$) and (0120) ($n = 5$) for 2D $(NpMA)_2(MA_{0.15}FA_{0.85})_{n-1}Pb_nI_{3n+1}$ perovskite, respectively. This result confirmed the successful integration of 2D perovskite into 3D perovskite from the lattice scale towards multidimensional regulation of perovskite solar cells for enhanced longevity.

The 1D perovskites were also widely used for multidimensional regulation of perovskite solar cells.[75,76] Figure 3(b) shows the microstructure of the 1D–3D perovskite heterostructure, which was obtained by HRTEM measurements. The junction region of hybrid 1D–3D, comprising 1D FAI-PbI_2-PZPY and 3D $Cs_{0.04}MA_{0.16}FA_{0.8}PbI_{0.85}Br_{0.15}$ perovskites, was clearly exhibited. The characteristic inter-planar spacing of 3.17 Å for the (200) plane of 3D perovskite and 4.87 Å for the (002) plane of 1D perovskite were determined, which confirmed the coexistence of 1D and 3D perovskites and the formation of heterostructure.

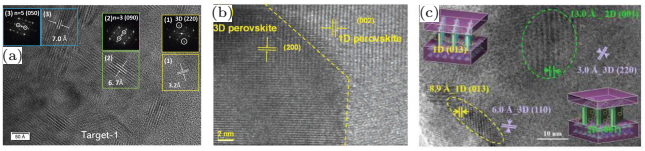


Fig. 3. (a) HRTEM images and FFT analysis of perovskite films incorporating NpMAI into the PbI_2 precursor solution, generating 2D–3D hybrid perovskite film. (b) HRTEM image of a 1D–3D perovskite heterostructure. (c) HRTEM image of a 1D–2D–3D hybrid perovskite film. Panel (a) is reproduced with permission from Ref. [69]. Panel (b) is reproduced with permission from Ref. [75]. Panel (c) is reproduced with permission from Ref. [77].

Simultaneous integration of both 1D and 2D perovskites into 3D perovskite was also reported.[77] HRTEM characterization was performed to explore the lattice matching in hybrid 1D–2D–3D perovskite heterostructures as shown in Fig. 3(c). In the control 3D $CsPbI_2Br$ perovskite, the spacing between planes was measured 3.0 Å for the (200) plane and 6.0 Å for the (100) plane, aligning with values derived from XRD analysis. Furthermore, two additional types of lattice fringes were observed: one with an interplane distance of 8.9 Å corresponding to the (013) plane of 1D-$Tpy_2Pb_3I_6$ and the other with 13.0 Å corresponding to the (001) plane of 2D-$TpyPb_3I_6$ perovskites. These observations were consistent with XRD findings.

4.2. Grain boundary modulation

Grain boundary passivation enabled by molecular additives was widely explored in the past few years.[13,78–90] TEM characterization was utilized to examine the intricate nanoscale configurations of P123-functionalized $MAPbI_3$ OIHP thin films.[86] Figures 4(a)–4(f) present a lower-magnification bright-field TEM image, illustrating the microstructure of the $MAPbI_3$-0.5P thin film. Notably, the crystalline $MAPbI_3$ grains or grain clusters and the P123-functionalized grain boundary (GB) walls are distinguished due to the bright contrast. HRTEM images of the $MAPbI_3$-0P, $MAPbI_3$-0.5P, $MAPbI_3$-1.0P, and $MAPbI_3$-10P thin films are depicted respectively. The P123-free $MAPbI_3$-0P thin film exhibits complete crystallinity without evident amorphous regions at GBs. In contrast, the P123-functionalized thin films conspicuously reveal the presence of P123-derived amorphous walls between the $MAPbI_3$ grains. The thickness of these walls increases with a higher concentration of P123. Similarly, another work using CPPA (fullerene derivative 4-(1′,5′-dihydro-1′-methyl-2′H-[5,6] fullereno-C60-Ih-[1,9-c]pyrrol-2′-yl) phenylphosphonic acid) as grain boundary modulator to consolidate the perovskite crystal structure

to enhance the tolerance against illumination, heat, and moisture, was reported.[79] More functionalized molecular additives were incorporated into perovskite films to facilitate facet orientation tailoring,[78] enhance device stability,[80,82,85,87] improve charge transfer across grain boundaries[81,84] and mitigate grain boundary issues.[83]

To enhance the stability of FA-based perovskite films, a novel strategy involving the encapsulation of each perovskite grain with nanoscale-thin layers of amorphous silica was proposed.[88] Characterization via TEM was conducted to unveil the microstructure within the FAPI–silica film. Figure 4(g) presents a bright-field TEM image of the FAPI–silica film. By analyzing the image contrast, distinct regions of perovskite grains (dark-contrast) and silica-based grain boundaries (light-contrast) were easily discerned. For a more detailed view, a higher magnification TEM image is provided in Fig. 4(h), offering clearer visualization of the amorphous silica and crystalline perovskite grains. The thickness of the amorphous silica layer was approximately 6 nm.

Perovskite grains with polycrystalline characteristics widely exist in perovskite solar cells.[13,89,90] Figure 4(i) depicts a cross-sectional HRTEM image of the $MAPbI_3$ capping layer within the mesoscopic-planar hybrid sample, revealing sizable $MAPbI_3$ perovskite grains.[13] The abrupt change in the orientation of lattice fringes serves as indicators for estimating the locations of grain boundaries (represented by dashed lines). The measured lattice-fringe spacings correspond to the (002) and (022) planes of the $MAPbI_3$ perovskite.

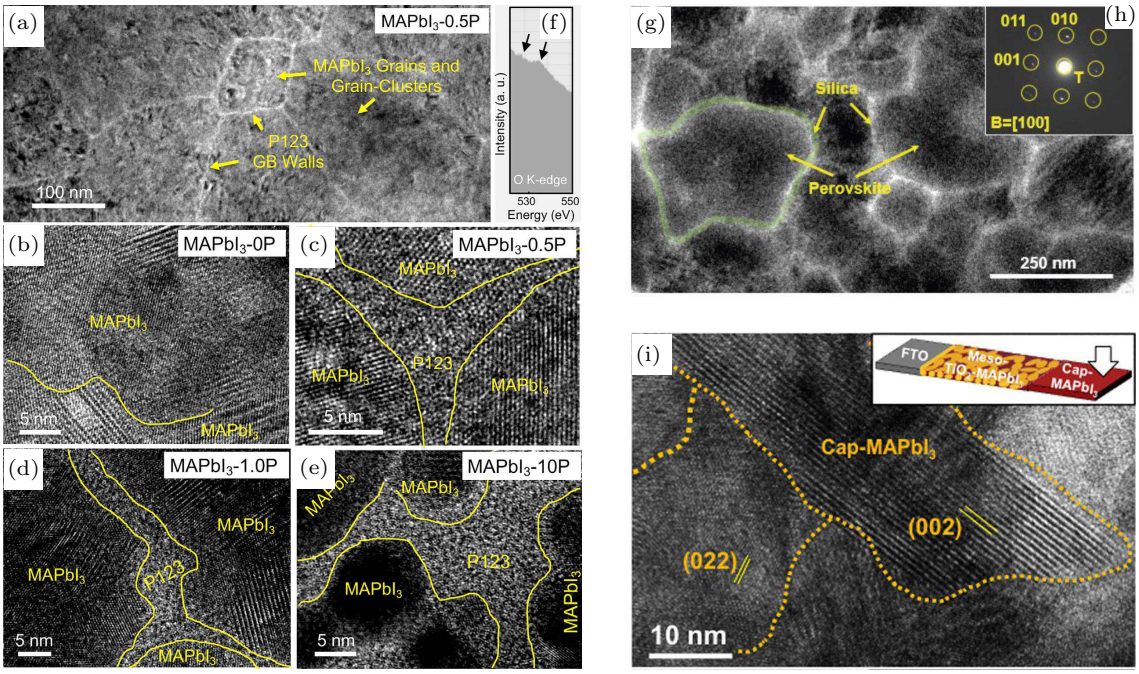


Fig. 4. (a) Low-magnification TEM image depicting the $MAPbI_3$-0.5P thin film. (b)–(e) HRTEM images of thin films: (b) $MAPbI_3$-0P, (c) $MAPbI_3$-0.5P, (d) $MAPbI_3$-1.0P, and (e) $MAPbI_3$-10P, with yellow lines delineating grain boundary regions. (f) EELS spectrum (O *K*-edge, indicated by arrows) obtained from the P123 region. (g) Bright-field TEM image showcasing the FAPI-TEOS film comprising silica-encapsulated perovskite grains, with one typical amorphous silica layer marked (light contrast). (h) SAED pattern of the center of a typical silica-encapsulated grain, illustrating its single-crystalline nature. (i) Cross-sectional HRTEM micrographs showing the $MAPbI_3$-capping layer in the mesoscopic-planar hybrid. Panels (a)–(f) are reproduced with permission from Ref. [86]. Panels (g) and (h) are reproduced with permission from Ref. [88]. Panel (i) is reproduced with permission from Ref. [13].

4.3. Phase segregation

Phase segregation limits the homogeneous distribution of band gap energies and electronic properties within perovskite grains.[11,15,16,91] For MHPs, phase inhomogeneity within a grain originating from phase segregation can be generated by inhomogeneous distribution of crystal structure,[92,93] A-site cation distribution,[10] molecular orientation[27] and halide composition.[11] Figure 5(a) shows the AC-TEM image of $CsPbBr_3$ perovskite. In this image, the detailed atomic structures in the lower region (marked as II) and upper region (marked as I) are different.[92] The contrast becomes particularly apparent when examining the Fourier transforms of regions I and II, as depicted in Figs. 5(b) and 5(c), respectively. Figures 5(d) and 5(e) offer simulations of the electron diffraction patterns for cubic and orthorhombic $CsPbBr_3$ in a [001] zone axis orientation. By comparing the experimental data with the simulations, a mixed structure scenario, region I crystallized in the cubic structure, whereas region II adopted the orthorhombic structure, is observed. The corresponding magnified images of regions I and II with atomic structures overlaid are shown in Figs. 5(f) and 5(g).

Inhomogeneous phase distribution caused by out-of-plane A-site cation segregation results in efficiency deficit in perovskite solar cells.[10] The potential influence of out-of-plane cation inhomogeneity on the perovskite lattice structure

can be observed through investigation into induced structural variations. The out-of-plane A-site compositional heterogeneity was visualized by examining lattice diversity across various perovskite phases. Cross-sectional TEM images were acquired to examine three distinct regions within the perovskite films: surface, bulk, and bottom. These regions were chosen to assess the interplanar spacing of the lattice (d), which serves as a direct indicator of phase heterogeneity. Comparison of the values of $d_{\{200\}}$ indicates vertical gradients in the cation distributions. In the reference film, the three measured interplanar spacing values were found to be $d_{\text{surface}} = 3.20$ Å, $d_{\text{bulk}} = 3.15$ Å, and $d_{\text{bottom}} = 3.11$ Å (Fig. 5(h)). In contrast, for the PSP-treated film, negligible variation of $d_{\text{surface}} = 3.13$ Å, $d_{\text{bulk}} = 3.13$ Å, and $d_{\text{bottom}} = 3.13$ Å was found (Fig. 5(i)). Accumulation of relatively smaller Cs atoms at the bottom of the reference film generates Cs-rich region therein and thus induces lattice mismatch and contraction, which brings about lattice strain.[94] Oppositely, the PSP treatment improves the alignment of the lattice in the out-of-plane direction and alleviates lattice stress by suppressing phase segregation.

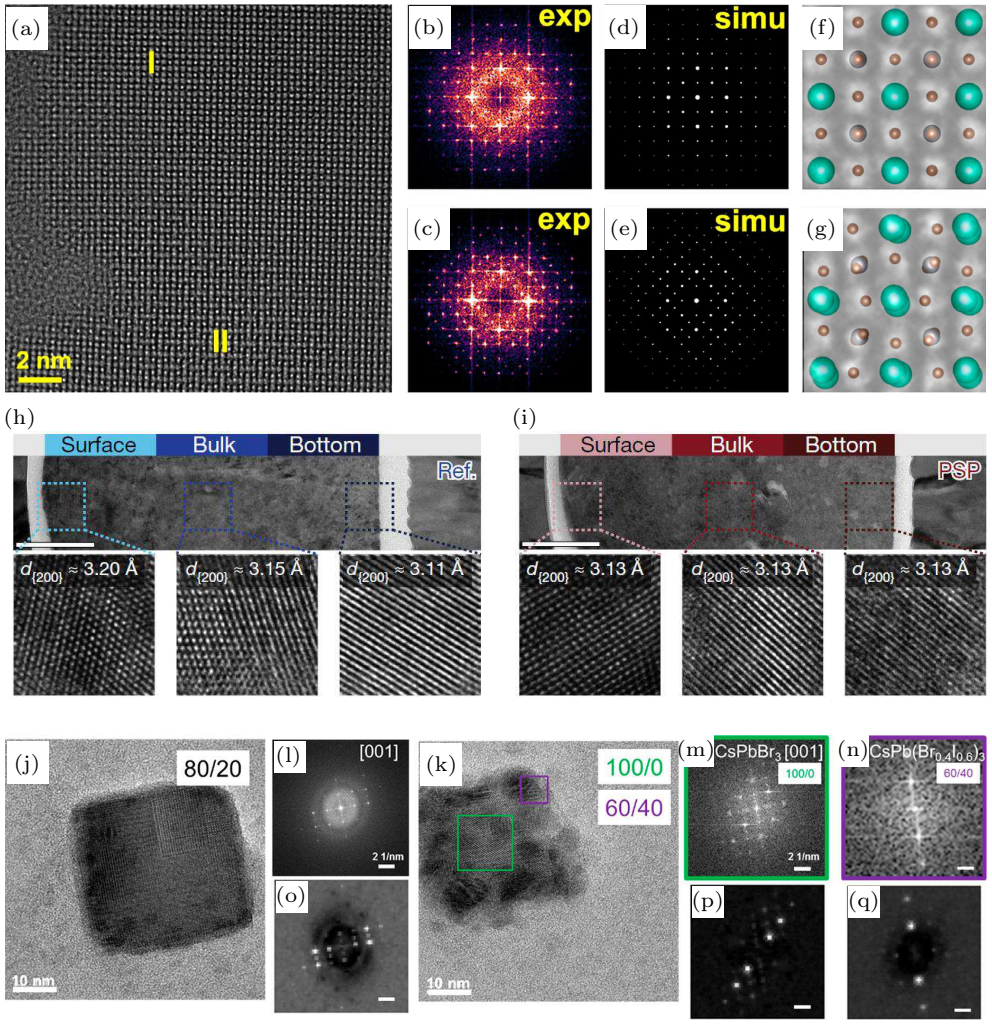


Fig. 5. (a) An experimental AC-HRTEM image featuring two designated regions, labeled as I and II. (b)–(c) Experimental Fourier transforms obtained from regions I (b) and II (c). (d)–(e) Simulated electron diffraction patterns for cubic (d) and orthorhombic (e) $CsPbBr_3$ structures. (f)–(g) Magnified images extracted from regions I (f) and II (g), with overlaid cubic and orthorhombic structure models, respectively. (h)–(i) HAADF TEM images of the reference CsFAMA perovskite device (h) and the PSP-treated CsFAMA perovskite device (i). (j)–(k) HRTEM micrograph displaying the initial structure of $CsPb(Br_{0.8}I_{0.2})_3$ and the same structure after 4 minutes of irradiation. (l) Diffraction pattern covering the entire area of panel (j). (m)–(n) Bromide-rich phase $CsPbBr_3$ extracted from inner and iodine-rich phase $CsPb(Br_{0.6}I_{0.4})_3$ from outer regions of interest of the particle, indicated with green and violet squares, respectively. (o)–(q) Diffraction patterns obtained via the algorithm corresponding to the FFTs shown in panels (l), (m), and (n). Panels (a)–(g) are reproduced with permission from Ref. [92]. Panels (h) and (i) are reproduced with permission from Ref. [10]. Panels (j)–(q) are reproduced with permission from Ref. [11].

In inorganic mixed halide perovskites, phase segregation can also occur due to the inhomogeneous distribution of halide composition when exposed to irradiation.[11] Using TEM images of both the whole and local regions of interest in the initial $CsPb(Br_{0.8}I_{0.2})_3$ perovskite, along with the corresponding FFT analysis (Figs. 5(j)–5(n)) and diffraction patterns generated by the algorithm aligned with the FFTs (Figs. 5(o)–5(q)), the initial structure was identified as $CsPb(Br_{0.8}I_{0.2})_3$. Following 4 minutes of electron-beam exposure, the phase within the center of the nanoparticle transitioned to $CsPbBr_3$, while the

phase observed near the boundary of the nanoparticle closely matched $CsPb(Br_{0.6}I_{0.4})_3$. These findings offer an atomistic depiction of phase segregation within grains, with iodide-rich phases occurring at grain boundaries and bromide-rich phases prevailing within the grain interior.

5. Degradation by electron beam, bias, heat and ambient factors induced microstructural inhomogeneity

Apart from intrinsic defects in the intragrain regions and surface/interface regions, and extrinsically introduced phase inhomogeneity in MHP thin films, structural inhomogeneity can also be induced by structural degradation/evolution. The degradation factors include electron beam exposure, bias, temperature (heat) and ambient conditions, which are discussed accordingly in this section.

5.1. Electron beam induced degradation

With an adequate irradiation dosage, degradation of $FAPbI_3$ exposed to electron beam can be observed.[12] Lower-magnification LAADF image of the pristine grain boundary could be observed after being scanned by a single electron beam accumulating a total dose of approximately 66 e/Å^2. Subsequent scans were also documented. By the third scan (around 200 e/Å^2), apparent changes in contrast within the perovskite structure were evident. After nine scans (about 600 e/Å^2), the perovskite structure was entirely depleted, giving way to a crystal structure characterized by uniform column intensities. With further extensive exposure (approximately 1333 e/Å^2), this phase underwent slight modification, resembling closely the 2H-hexagonal PbI_2 phase.

Accumulation of electron dose can also cause large scale cracks on perovskite thin films.[95] Bright field TEM showed that the contrast of individual $MAPbI_3$ grain was changed with weak electron exposure (Figs. 6(a) and 6(b)). After 1 minute of mild electron beam exposure, the disappearance of twin domains led to a more consistent contrast within $MAPbI_3$ grains. Moreover, cracks emerged initially at grain boundaries and subsequently propagated across the film with continued exposure to weak electron beams (Figs. 6(c)–6(h)), aligning with a reduction in unit cell volume as suggested by the decreased lattice spacing.

The structural and microstructural evolution of triplication double-halide perovskite material $Cs_{0.05}MA_{0.10}FA_{0.85}Pb(I_{0.85}Br_{0.15})_3$ was reported. The observation by HAADF-STEM revealed the formation of PbI_2 nanoparticles at the perovskite-substrate interface and at grain boundaries (Figs. 6(i)–6(k)).[96] Sustained electron beam irradiation induced irreversible damage, leading to the formation of PbI_2 nanoparticles and the desorption and evaporation of I_2, likely through the reduction of PbI_2 to metallic Pb. Evolution of $CsPbBr_3$ nanocuboids was also evidenced by HAADF-STEM images by increasing the electron dose at −60 °C from 1.8×10^3 e^-/Å^2 to 7.2×10^4 e^-/Å^2.[97] Another research about the electron beam-induced structural evolution of $FAPbI_3$ showed that the superstructure with ordered I and FA vacancies along $\langle110\rangle_c$ direction was formed as evidenced by diffraction patterns.[98] More electron beam induced formation of defects and structural transformations were reported.[12,99–103]

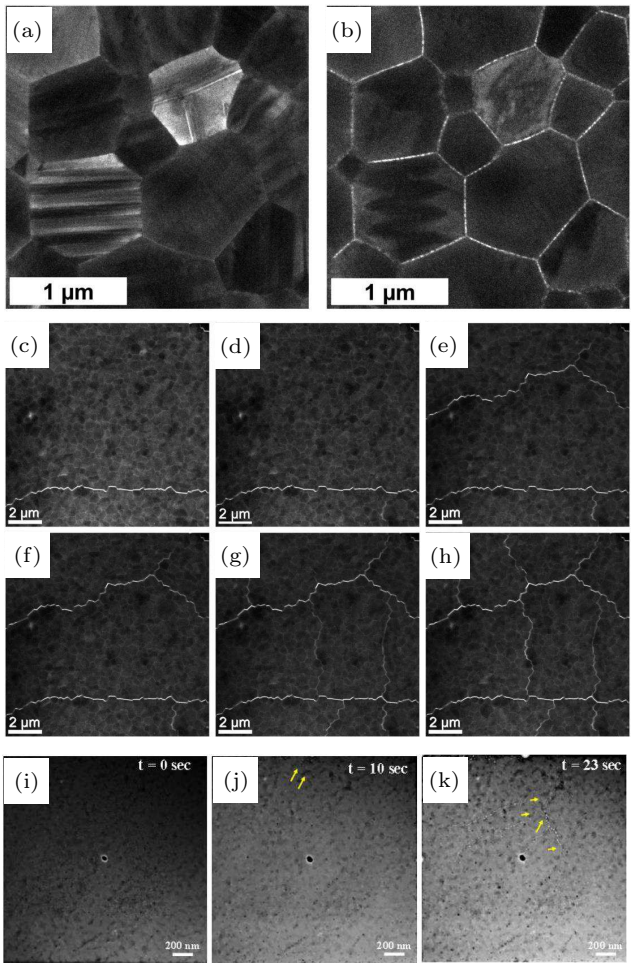


Fig. 6. Bright-field TEM images of a $CH_3NH_3PbI_3$ thin film after (a) brief, low-dose electron exposure and (b) 1 minute of exposure with a dose rate of ~ 2 $e\cdot$Å$^{-2}\cdot$s^{-1}. Lower magnification images of the same sample exposed for (c) 2 minutes, (d) 3 minutes, (e) 4 minutes, (f) 5 minutes, (g) 6 minutes, and (h) 8 minutes using the same dose rate of ~ 2 $e\cdot$Å$^{-2}\cdot$s^{-1}. (i) Freshly prepared perovskite films. (j)–(k) Initial appearance and propagation of PbI_2 particles. Yellow arrows indicate the path of PbI_2 formation propagation. Panels (a)–(h) are reproduced with permission from Ref. [95]. Panels (i)–(k) are reproduced with permission from Ref. [96].

5.2. Bias induced degradation

Applying bias to the MHPs is another origin of structural decomposition.[40,104,105] Sequential HRTEM images of $FAPbI_3$ perovskite under 1 V electrical bias for 5 min are shown in Fig. 7(a).[104] The lattice fringes of perovskite crystals observed at 0 seconds gradually faded away and were entirely absent after 300 seconds of continuous 1 V forward bias. The real-time fading of these specific lattice fringes under electrical bias suggested the amorphization of perovskite

nanocrystals. However, the lattice fringes in the red boxes remained crystalline characteristics after being treated with bias. The *d*-spacing of the lattice fringes in the red boxes was consistent with the (001) plane of PbI_2 (6.96 Å), which suggested that only the $FAPbI_3$ phase underwent amorphization with bias treatment. Similar structural decomposition under bias can be observed in $MAPbI_3$.[105]

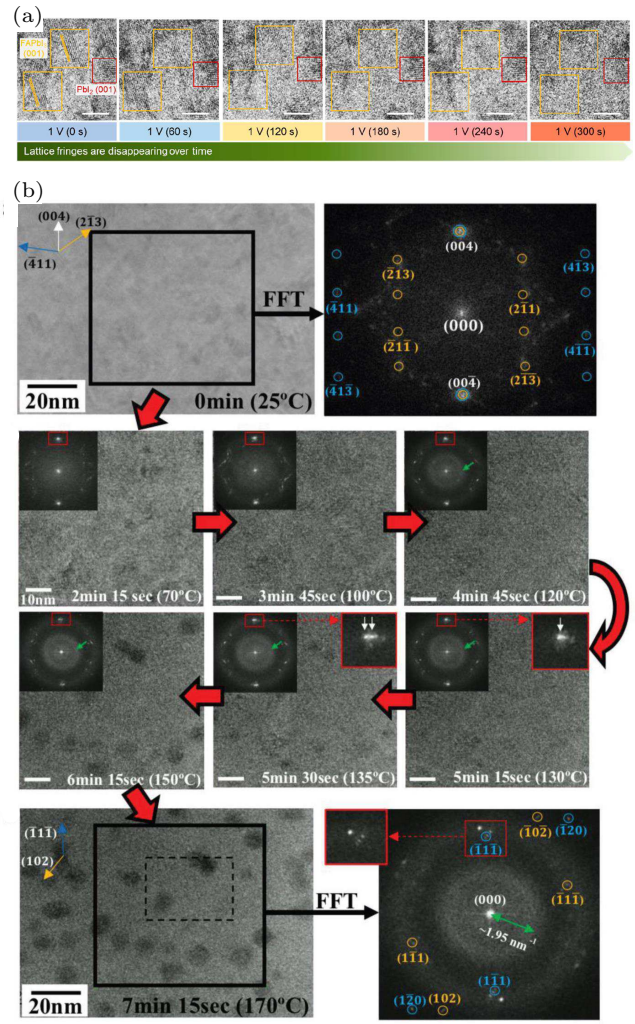


Fig. 7. (a) Series of HRTEM images depicting perovskite materials under a 1 V electrical bias. The initial lattice fringes of perovskite are highlighted in yellow boxes, while those of lead iodide are highlighted in the red box. (b) HRTEM images and FFTs depict the intricate stages of thermal degradation ranging from 25 °C to 170 °C. The first panel shows an HRTEM image and its corresponding FFT of the $MAPbI_3$ layer, revealing various crystallographic orientations at 25 °C. The second and third panels display HRTEM images and FFTs captured from an *in situ* HRTEM video, elucidating the intermediate processes in detail. The fourth panel showcases an HRTEM image, revealing black dots alongside its FFT, which encompasses both spot diffraction and broad ring patterns observed at 170 °C. Panel (a) is reproduced with permission from Ref. [104]. Panel (b) is reproduced with permission from Ref. [111].

5.3. Heat induced degradation

Heat-induced degradation is another common factor that brings about inhomogeneity in MHPs.[101,106–109] Cross-sectional views of evolution of $MAPbI_3$ devices fabricated in vacuum, glovebox, air and single step with increased temperatures obtained by the STEM-HAADF images demonstrated no observable change in the perovskite layer, even with heating up to 150 °C.[110] For sample C that was fabricated in air, obvious change in the perovskite layer was observed after the sample being heated to 150 °C. The bright regions close to interface with titanic scaffold underwent formation of holes, which was assumed to be due to the usage of warm air flow in the process of drying PbI_2 layer that introduced low amount of O_2 and H_2O. Further increasing the temperature led to the degradation of perovskite layers and the formation of PbI_2 at the interface with FTO layers with further migration and coalesce in samples A, B and D, which was not observed in sample C because of different degradation dynamics between them. As the temperature continued to rise until 250 °C, the perovskite component of all samples vanished within minutes.

Another research showed similar degradation of the $MAPbI_3$ perovskite. Some black dots appear in the $MAPbI_3$ layer as the temperature rises from 25 °C to 170 °C, as shown in Fig. 7(b).[111] Such black dots indicate the structural evolution and the formation of defects in $MAPbI_3$ layer. FFT analysis exhibits both spot diffraction pattern and broad ring pattern which corresponds to structural amorphization.

5.4. Ambient factors induced degradation

Environmental factors besides heat, such as water and light, were studied regarding their influence on perovskite degradation.[107,112–116] The chemical transformation from $MAPbI_3$ to $MAPbI_3{\cdot}H_2O$ was elucidated through *in situ* TEM experiments showing live observations of perovskite solar cells under humidity (Fig. 8(a)).[112] Figure 8(b) depicts a precise and dynamic evaluation of the reaction mechanisms concerning PbI_2 formation at the nanoscale. PbI_2 formation proceeded through the nanoscale dissolution of $MAPbI_3{\cdot}H_2O$ followed by the recrystallization of larger PbI_2 particles with a preference for elongation in one direction, resulting in the formation of elongated PbI_2 particles.

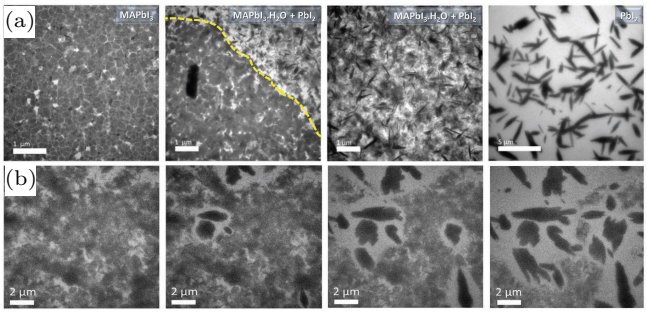


Fig. 8. (a) *In situ* TEM utilizing liquid cell Poseidon protochips showcasing the transformation of $MAPbI_3$ into $MAPbI_3{\cdot}H_2O$ and PbI_2. (b) Higher magnification displaying the dissolution of $MAPbI_3{\cdot}H_2O$ and its recrystallization into PbI_2. Panels (a) and (b) are reproduced with permission from Ref. [112].

Light can also induce structural evolution and decomposition of perovskites. SER measurements of $Cs_{0.05}FA_{0.78}MA_{0.17}Pb(I_{0.83}Br_{0.17})_3$ thin films before and after one hour of illumination revealed that in FA-rich per-

ovskite region, even trace amounts of nanoscale phase impurities, such as hexagonal polytype and lead iodide inclusions, serve not only as traps for photoexcited carriers but also as sites where the photochemical degradation of the absorber layer is initiated.[114] Another research using on-chip light-incorporated *in situ* transmission electron microscopy (LI^{2}ST) approach also demonstrated decomposition of polycrystalline MHP film under continuous light illumination, which initiated and spread within the intragrain regions instead of at the grain boundaries.[113]

6. Conclusion

In conclusion, the application of TEM and STEM in the study of MHPs offers invaluable insights into the factors influencing device performance. The microstructural inhomogeneity in MHPs plays a crucial role in affecting the efficiency and stability of MHP-based devices. This inhomogeneity manifests through various structural deviations, encompassing defects such as intragrain line defects, planar defects, point defects, and surface/interface defects. Additionally, structural variations in MHPs, not necessarily attributable to defect formation, further complicate device performance through multi-dimensional regulation, grain boundary modulation, and phase segregation in MHP solar cells. TEM and STEM techniques excel in unraveling the atom-scale complexity of these heterogeneous regions, providing essential information for designing strategies to mitigate their adverse effects. However, deeper understanding of defects at surface and interface of MHP devices by TEM techniques still needs to be revealed in terms of types and distributions of defects at grain boundaries, interfaces, and within the bulk of MHP materials, while identifying these defects with high-resolution imaging and low beam-induced damage remains challenging. In addition, being able to capture phase transitions and dynamic processes such as ion migration in MHPs under different environmental conditions is beneficial for investigating the stability issue, which requires advanced *in situ* TEM techniques capable of high-speed imaging. Being able to obtain such detailed and transient information about the MHP microstructures is beneficial for targeted modulations to enhance the efficiency and stability of MHP-based technologies.

References

[1] Zhu H, Teale S, Lintangpradipto M N, Mahesh S, Chen B, McGehee M D, Sargent E H and Bakr O M 2023 *Nat. Rev. Mater.* **8** 569
[2] Liu D, Luo D, Iqbal A N, Orr K W P, Doherty T A S, Lu Z, Stranks S D and Zhang W 2021 *Nat. Mater.* **20** 1337
[3] Liu X, Luo D, Lu Z H, Yun J, Saliba M, Seok S I and Zhang W 2023 *Nat. Rev. Chem.* **7** 462
[4] Ma D, Lin K, Dong Y, Choubisa H, Proppe A H, Wu D, Wang Y K, Chen B, Li P, Fan J, Yuan F, Johnston A, Liu Y, Kang Y, Lu Z, Wei Z and Sargent E H 2021 *Nature* **599** 594
[5] Fakharuddin A, Gangishetty M K, Abdi-Jalebi M, Chin S, Yusoff A R, Congreve D N, Tress W, Deschler F, Vasilopoulou M and Bolink H J 2022 *Nat. Electron.* **5** 203
[6] Pacchioni G 2021 *Nat. Rev. Mater.* **6** 108
[7] Zhang Y, Ma Y, Wang Y, Zhang X, Zuo C, Shen L and Ding L 2021 *Adv. Mater.* **33** 2006691
[8] Jing H, Peng R, Ma R, He J, Zhou Y, Yang Z, Li C, Liu Y, Guo X, Zhu Y, Wang D, Su J, Sun C, Bao W and Wang M 2020 *Nano Lett.* **20** 7144
[9] Wang H, Li S, Liu X, Shi Z, Fang X and He J 2021 *Adv. Mater.* **33** 2003309
[10] Liang Z, Zhang Y, Xu H, Chen W, Liu B, Zhang J, Zhang H, Wang Z, Kang D, Zeng J, Gao X, Wang Q, Hu H, Zhou H, Cai X, Tian X, Reiss P, Xu B, Kirchartz T, Xiao Z, Dai S, Park N G, Ye J and Pan X 2023 *Nature* **624** 557
[11] Funk H, Shargaieva O, Eljarrat A, Unger E L, Koch C T and AbouRas D 2020 *J. Phys. Chem. Lett.* **11** 4945
[12] Rothmann M U, Kim J S, Borchert J, Lohmann K B, O'Leary C M, Sheader A A, Clark L, Snaith H J, Johnston M B and Nellist P D 2020 *Science* **370** eabb5940
[13] Zhou Y, Vasiliev A L, Wu W, Yang M, Pang S, Zhu K and Padture N P 2015 *J. Phys. Chem. Lett.* **6** 2292
[14] Ji F, Pang S, Zhang L, Zong Y, Cui G, Padture N P and Zhou Y 2017 *ACS Energy Lett.* **2** 2727
[15] Yu Y, Zhang D and Yang P 2017 *Nano Lett.* **17** 5489
[16] Jones T W, Osherov A, Alsari M, Sponseller M, Duck B C, Jung Y K, Settens C, Niroui F, Brenes R, Stan C V, Li Y, Abdi-Jalebi M, Tamura N, Macdonald J, Burghammer M, Friend R H, Bulovic V, Walsh A, Wilson G J, Lilliu S and Stranks S D 2019 *Energy Environ. Sci.* **12** 596
[17] RegaladoPérez E, DíazCruz E B, LandaBautista J, Mathews N R and Mathew X 2021 *ACS Appl. Mater. Inter.* **13** 11833
[18] ElHajje G, Momblona C, GilEscrig L, Ávila J, Guillemot T, Guillemoles J F, Sessolo M, Bolink H J and Lombez L 2016 *Energy Environ. Sci.* **9** 2286
[19] Tailor N K, Yukta Ranjan R, Ranjan S, Sharma T, Singh A, Garg A, Nalwa K S, Gupta R K and Satapathi S 2021 *J. Mater. Chem. A* **9** 21551
[20] Tennyson E M, Doherty T A S and Stranks S D 2019 *Nat. Rev. Mater.* **4** 573
[21] Chen S and Gao P 2020 *J. Appl. Phys.* **128** 010901
[22] Song K, Liu L, Zhang D, Hautzinger M P, Jin S and Han Y 2020 *Adv. Energy Mater.* **10** 1904006
[23] Zhou Y, Sternlicht H, and Padture N P 2019 *Joule* **3** 641
[24] Fan Z, Xiao H, Wang Y, Zhao Z, Lin Z, Cheng H C, Lee S J, Wang G, Feng Z and Goddard W A 2017 *Joule* **1** 548
[25] Wang W, Ma Y, and Qi L 2017 *Adv. Funct. Mater.* **27** 1603653
[26] Zhu Y, Gui Z, Wang Q, Meng F, Feng S, Han B, Wang P, Huang L, Wang H and Gu M 2020 *Nano Energy* **73** 104820
[27] Zhang D, Zhu Y, Liu L, Ying X, Hsiung C E, Sougrat R, Li K and Han Y 2018 *Science* **359** 675
[28] Xiao Z, Zhao L, Tran N L, Lin Y L, Silver S H, Kerner R A, Yao N, Kahn A, Scholes G D and Rand B P 2017 *Nano Lett.* **17** 6863
[29] Shamsi J, Dang Z, Bianchini P, Canale C, Di Stasio F, Brescia R, Prato M and Manna L 2016 *J. Am. Chem. Soc.* **138** 7240
[30] Shi E, Yuan B, Shiring S B, Gao Y, Akriti Guo Y, Su C, Lai M, Yang P and Kong J 2020 *Nature* **580** 614
[31] Akhavan Kazemi M A, Raval P, Cherednichekno K, Chotard J N, Krishna A, Demortiere A, Reddy G M and Sauvage F 2021 *Small Methods* **5** 2000834
[32] Li Y, Zhou W, Li Y, Huang W, Zhang Z, Chen G, Wang H, Wu G H, Rolston N and Vila R 2019 *Joule* **3** 2854
[33] Tong Y, Fu M, Bladt E, Huang H, Richter A F, Wang K, Müller-Buschbaum P, Bals S, Tamarat P and Lounis B 2018 *Angew. Chem. Int. Ed.* **130** 16326
[34] Tong Y, Bladt E, Aygüler M F, Manzi A, Milowska K Z, Hintermayr V A, Docampo P, Bals S, Urban A S and Polavarapu L 2016 *Angew. Chem. Int. Ed.* **55** 13887
[35] Ma M, Zhang X, Xu L, Chen X, Wang L, Cheng T, Wei F, Yuan J and Shen B 2023 *Adv. Mater.* **35** 2300653
[36] Ma M, Zhang X, Chen X, Xiong H, Xu L, Cheng T, Yuan J, Wei F and Shen B 2023 *Nat. Commun.* **14** 7142
[37] Zheng F, Chen W, Bu T, Ghiggino K P, Huang F, Cheng Y, Tapping P, Kee T W, Jia B and Wen X 2019 *Adv. Energy Mater.* **9** 1901016
[38] Matteocci F, Busby Y, Pireaux J J, Divitini G, Cacovich S, Ducati C and Di Carlo A 2015 *ACS Appl. Mater. Inter.* **7** 26176
[39] Jung H J, Kim D, Kim S, Park J, Dravid V P and Shin B 2018 *Adv. Mater.* **30** 1802769
[40] Deng Y H 2021 *Nature* **594** E6
[41] Xiang T, Zhang Y, Wu H, Li J, Yang L, Wang K, Xia J, Deng Z, Xiao J and Li W 2020 *Sol. Energy Materials Sol. Cells* **206** 110317

[42] Jiang J, Sun X, Chen X, Wang B, Chen Z, Hu Y, Guo Y, Zhang L, Ma Y and Gao L 2019 *Nat. Commun.* **10** 4885

[43] Wu X, Gao D, Sun X, Zhang S, Wang Q, Li B, Li Z, Qin M, Jiang X and Zhang C 2023 *Adv. Mater.* **35** 2208431

[44] Yuan B and Yu Y 2022 *Chem* **8** 327

[45] Zhu Y, Wang S, Li B, Yang X, Wu D, Feng S, Li L, Rogach A L and Gu M 2021 *J. Phys. Chem. Lett.* **12** 12187

[46] Pham H T, Yin Y, Andersson G, Weber K J, Duong T and WongLeung J 2021 *Nano Energy* **87** 106226

[47] Zhi R, Yang C, Rothmann M U, Du H, Jiang Y, Xu Y, Yin Z, Mo Y, Dong W and Liang G 2023 *ACS Energy Lett.* **8** 2620

[48] Jiang Y, Du H, Zhi R, Rothmann M U, Wang Y, Wang C, Liang G, Hu Z, Cheng Y and Li W 2024 *Adv. Mater.* **36** 2312157

[49] Cai S, Dai J, Shao Z, Rothmann M U, Jia Y, Gao C, Hao M, Pang S, Wang P, Lau S P, Zhu K, Berry J J, Herz L M, Zeng X and Zhou Y 2022 *J. Am. Chem. Soc.* **144** 1910

[50] Tan C S, Hou Y, Saidaminov M I, Proppe A, Huang Y, Zhao Y, Wei M, Walters G, Wang Z and Zhao Y 2020 *Adv. Sci.* **7** 1903166

[51] Rothmann M U, Li W, Zhu Y, Bach U, Spiccia L, Etheridge J and Cheng Y 2017 *Nat. Commun.* **8** 14547

[52] Li W, Rothmann M U, Zhu Y, Chen W, Yang C, Yuan Y, Choo Y Y, Wen X, Cheng Y and Bach U 2021 *Nat. Energy* **6** 624

[53] Thind A S, Luo G, Hachtel J A, Morrell M V, Cho S B, Borisevich A Y, Idrobo J C, Xing Y and Mishra R 2019 *Adv. Mater.* **31** 1805047

[54] Akkerman Q A, Bladt E, Petralanda U, Dang Z, Sartori E, Baranov D, Abdelhady A L, Infante I, Bals S and Manna L 2019 *Chem. Mater.* **31** 2182

[55] Song K, Liu J, Qi D, Lu N and Qin W 2022 *J. Phys. Chem. Lett.* **13** 2117

[56] Yesudhas S, Morrell M V, Anderson M J, Ullrich C A, KenneyBenson C, Xing Y and Guha S 2019 *Chem. Mater.* **32** 785

[57] Xu W, Liu J, Dong B, Huang J, Shi H, Xue X and Liu M 2023 *Sci. Adv.* **9** eadi7931

[58] Milstein T J, Roh J Y D, Jacoby L M, Crane M J, Sommer D E, Dunham S T and Gamelin D R 2022 *Chem. Mater.* **34** 3759

[59] He Z, Tang Q, Liu X, Yan X, Li K and Yue D 2021 *Energy & Fuels* **35** 15005

[60] Li F, Liu Y, Wang H, Zhan Q, Liu Q and Xia Z 2018 *Chem. Mater.* **30** 8546

[61] Doherty T A, Winchester A J, Macpherson S, Johnstone D N, Pareek V, Tennyson E M, Kosar S, Kosasih F U, Anaya M and AbdiJalebi M 2020 *Nature* **580** 360

[62] Liu J, Song K, Zheng X, Yin J, Yao K, X, Chen C, Yang H, Hedhili M N, Zhang W and Han P 2021 *J. Phys. Chem. Lett.* **12** 10402

[63] Zhao L, Shi Z, Zhou Y, Wang X, Xian Y, Dong Y, Reid O, Ni Z, Beard M C, Yan Y and Huang J 2024 *Nat. Photonics* **18** 250

[64] Jiang Q, Tong J, Xian Y, Kerner R A, Dunfield S P, Xiao C, Scheidt R A, Kuciauskas D, Wang X, Hautzinger M P, Tirawat R, Beard M C, Fenning D P, Berry J J, Larson B W, Yan Y and Zhu K 2022 *Nature* **611** 278

[65] Chen L, Li C, Xian Y, Fu S, Abudulimu A, Li D, Friedl J D, Li Y, Neupane S, Tumusange M S, Sun N, Wang X, Ellingson R J, Heben M J, Podraza N J, Song Z and Yan Y 2023 *Adv. Energy Mater.* **13** 2301218

[66] Li C, Wang X, Bi E, Jiang F, Park S M, Li Y, Chen L, Wang Z, Zeng L, Chen H, Liu Y, Grice C R, Abudulimu A, Chung J, Xian Y, Zhu T, Lai H, Chen B, Ellingson R J, Fu F, Ginger D S, Song Z, Sargent E H and Yan Y 2023 *Science* **379** 690

[67] Yao Q, Xue Q, Li Z, Zhang K, Zhang T, Li N, Yang S, Brabec C J, Yip H and Cao Y 2020 *Adv. Mater.* **32** 2000571

[68] Gu H, Liang C, Xia Y, Wei Q, Liu T, Yang Y, Hui W, Chen H, Niu T, Chao L, Wu Z, Xie X, Qiu J, Shao G, Gao X, Xing G, Chen Y and Huang W 2019 *Nano Energy* **65** 104050

[69] Zhou T, Xu Z, Wang R, Dong X, Fu Q and Liu Y 2022 *Adv. Mater.* **34** 2200705

[70] Zhang C, Wu S, Tao L, Arumugam G M, Liu C, Wang Z, Zhu S, Yang Y, Lin J, Liu X, Schropp R and Mai Y 2020 *Adv. Energy Mater.* **10** 2002004

[71] Zhu Z, Zhu C, Yang L, Chen Q, Zhang L, Dai J, Cao J, Zeng S, Wang Z, Wang Z, Zhang W, Bao J, Yang L, Yang Y, Chen B, Yin C, Chen H, Cao Y, Gu H, Yan J, Wang N, Xing G, Li H, Wang X, Li S, Liu Z, Zhang H, Wang L, Huang X and Huang W 2022 *Nat. Mater.* **21** 1042

[72] Azmi R, Ugur E, Seitkhan A, Aljamaan F, Subbiah A S, Liu J, Harrison G T, Nugraha M I, Eswaran M K, Babics M, Chen Y, Xu F, Allen T, Rehman A, Wang C, Anthopoulos T D, Schwingenschlogl U, Bastiani M, Aydin E and De Wolf S 2022 *Science* **376** 73

[73] Liu T, Guo J, Lu D, Xu Z, Fu Q, Zheng N, Xie Z, Wan X, Zhang X, Liu Y and Chen Y 2021 *ACS Nano* **15** 7811

[74] Li H, Zhang C, Gong C, Zhang D, Zhang H, Zhuang Q, Yu X, Gong S, Chen X, Yang J, Li X, Li R, Li J, Zhou J, Yang H, Lin Q, Chu J, Gratzel M, Chen J and Zang Z 2023 *Nat. Energy* **8** 946

[75] Fan J, Ma Y, Zhang C, Liu C, Li W, Schropp R E I and Mai Y 2018 *Adv. Energy Mater.* **8** 1703421

[76] Kong T, Xie H, Zhang Y, Song J, Li Y, Lim E L, Hagfeldt A and Bi D 2021 *Adv. Energy Mater.* **11** 2101018

[77] Liu K, Yuan S, Xian Y, Long Y, Yao Q, Rahman N U, Guo Y, Sun M, Xue Q, Yip H, Cabot A, Li W and Fan J 2021 *Small* **17** 2100888

[78] Luo C, Zheng G, Gao F, Wang X, Zhao Y, Gao X and Zhao Q 2022 *Joule* **6** 240

[79] You S, Zeng H, Liu Y, Han B, Li M, Li L, Zheng X, Guo R, Luo L, Li Z, Zhang C, Liu R, Zaho Y, Zahng S, Peng Q, Wang T, Chen Q, Eickemeyer F T, Carlson B, Zakeeruddin S M, Mai L, Rong Y, Gratzel M and Li X 2023 *Science* **379** 288

[80] Han B, Yuan S, Cai B, Song J, Liu W, Zhang F, Fang T, Wei C and Zeng H 2021 *Adv. Funct. Mater.* **31** 2011003

[81] Son D Y, Lee J W, Choi Y J, Jang I H, Lee S, Yoo P J, Shin H, Ahn N, Choi M, Kim D and Park N G 2016 *Nat. Energy* **1** 16081

[82] Chen Z, Cheng Q, Chen H, Wu Y, Ding J, Wu X, Yang H, Liu H, Chen W, Tang X, Lu X, Li Y and Li Y 2023 *Adv. Mater.* **35** 2300513

[83] Zhao L, Tang P, Luo D, Dar M I, Eickemeyer F T, Arora N, Hu Q, Luo J, Liu Y, Zakeeruddin S M, Hagfeldt A, Arbiol J, Hunag W, Gong Q, Russell T P, Friend R H, Gratzel M and Zhu R 2022 *Sci. Adv.* **8** eabo3733

[84] Wang F, Li M, Tian Q, Sun R, Ma H, Wang H, Chang J, Li Z, Chen H, Cao J, Wang A, Dong J, Liu Y, Zhao J, Chu Y, Yan S, Wu Z, Liu J, Li Y, Chen X, Gao P, sun Y, Liu T, Liu W, Li R, Wang J, Cheng Y, Liu X, Huang W and Qin T 2023 *Nat. Commun.* **14** 3216

[85] Zhao Y, Zhu P, Wang M, Huang S, Zhao Z, Tan S, Han T H, Lee J W, Huang T, Wang R, Xue J, Meng D, Huang Y, Marian J, Zhu J and Yang Y 2020 *Adv. Mater.* **32** 1907769

[86] Zong Y, Zhou Y, Zhang Y, Li Z, Zhang L, Ju M, Chen M, Pang S, Zeng X and Padture N P 2018 *Chem* **4** 1404

[87] Li X, Zhang W, Zhang W, Wang H Q and Fang J 2019 *Nano Energy* **58** 825

[88] Liu T, Zhou Y, Li Z, Zhang L, Ju M, Luo D, Yang Y, Yang M, Kim D H, Yang W, Padture N P, Beard M C, Zeng X, Zhu K, Gong Q and Zhu R 2018 *Adv. Energy Mater.* **8** 1800232

[89] Choi J, Song S, Höantner M T, Snaith H J and Park T 2016 *ACS Nano* **10** 6029

[90] Lin Y, Liu Y, Chen S, Wang S, Ni Z, Van Brackle C, H, Yang S, Zhao J, Yu Z, Dai X, Wang Q, Deng Y and Huang J 2021 *Energy Environ. Sci.* **14** 1563

[91] Xiao M, Huang F, Huang W, Dkhissi Y, Zhu Y, Etheridge J, GrayWeale A, Bach U, Cheng Y and Spiccia L 2014 *Angew. Chem. Int. Ed.* **53** 9898

[92] Yu Y, Zhang D, Kisielowski C, Dou L, Kornienko N, Bekenstein Y, Wong A B, Alivisatos A P and Yang P 2016 *Nano Lett.* **16** 7530

[93] Kim T W, Uchida S, Matsushita T, Cojocaru L, Jono R, Kimura K, Matsubara D, Shirai M, Ito K, Matsumoto H, Kondo T and Segawa H 2018 *Adv. Mater.* **30** 1705230

[94] TurrenCruz S H, Hagfeldt A and Saliba M 2018 *Science* **362** 449

[95] Rothmann M U, Li W, Zhu Y, Liu A, Ku Z, Bach U, Etheridge J and Cheng Y 2018 *Adv. Mater.* **30** 1800629

[96] Manekkathodi A, Marzouk A, Ponraj J, Belaidi A and Ashhab S 2020 *ACS Appl. Energy Mater.* **3** 6302

[97] Dang Z, Shamsi J, Akkerman Q A, Imran M, Bertoni G, Brescia R and Manna L 2017 *ACS Omega* **2** 5660

[98] Yang C, Zhi R, Rothmann M U, Xu Y, Li L, Hu Z, Pang S, Cheng Y, Van Tendeloo G and Li W 2023 *Adv. Mater.* **35** 2211207

[99] Alberti A, Bongiorno C, Smecca E, Deretzis I, La Magna A and Spinella C 2019 *Nat. Commun.* **10** 2196

[100] Jacobsson T J, CorreaBaena J P, Halvani Anaraki E, Philippe B, Stranks S D, Bouduban M E, Tress W, Schenk K, Teuscher J and Moser J E 2016 *J. Am. Chem. Soc.* **138** 10331

[101] Dang Z, Shamsi J, Palazon F, Imran M, Akkerman Q A, Park S, Bertoni G, Prato M, Brescia R and Manna L 2017 *ACS Nano* **11** 2124

[102] Zhou X, Yang C, Sang X, Li W, Wang L, Yin Z, Han J, Li Y, Ke X and Hu Z 2021 *J. Phys. Chem. C* **125** 10786
[103] Xi J, Xi K, Sadhanala A, Zhang K, Li G, Dong H, Lei T, Yuan F, Ran C and Jiao B 2019 *Nano Energy* **56** 741
[104] Kim M C, Ahn N, Cheng D, Xu M, Ham S Y, Pan X, Kim S J, Luo Y, Fenning D P and Tan D H 2021 *ACS Energy Lett.* **6** 3530
[105] Jeangros Q, Duchamp M, Werner J R M, Kruth M, DuninBorkowski R E, Niesen B, Ballif C and HesslerWyser A 2016 *Nano Lett.* **16** 7013
[106] Seo Y H, Kim J H, Kim D H, Chung H S and Na S I 2020 *Nano Energy* **77** 105164
[107] Yang B, Dyck O, Ming W, Du M, H, Das S, Rouleau C M, Duscher G, Geohegan D B and Xiao K 2016 *ACS Appl. Mater. Inter.* **8** 32333
[108] Du T, Burgess C H, Lin C T, Eisner F, Kim J, Xu S, Kang H, Durrant J R and McLachlan M A 2018 *Adv. Funct. Mater.* **28** 1803943
[109] Aguiar J A, Wozny S, Holesinger T G, Aoki T, Patel M K, Yang M, Berry J J, AlJassim M, Zhou W and Zhu K 2016 *Energy Environ. Sci.* **9** 2372
[110] Divitini G, Cacovich S, Matteocci F, Cin'a L, Di Carlo A and Ducati C 2016 *Nat. Energy* **1** 16
[111] Kim T W, Shibayama N, Cojocaru L, Uchida S, Kondo T and Segawa H 2018 *Adv. Funct. Mater.* **28** 1804039
[112] Akhavan Kazemi M A, Raval P, Cherednichekno K, Chotard J N, Krishna A, Demortiere A, Reddy G N M and Sauvage F 2021 *Small Methods* **5** 2000834
[113] Duan T, Wang W, Cai S and Zhou Y 2023 *ACS Energy Lett.* **8** 3048
[114] Macpherson S, Doherty T A S, Winchester A J, Kosar S, Johnstone D N, Chiang Y H, Galkowski K, Anaya M, Frohna K, Iqbal A N, Negane S, Roose B, Andaji-Garmaroudi Z, Orr K W P, Parker J E, Midgley P A, Dani K M and Stranks S D 2022 *Nature* **607** 294
[115] Ko Y H, Prabhakaran P, Jalalah M, Lee S J, Lee K S and Park J G 2018 *J. Mater. Chem. C* **6** 7803
[116] Woo J Y, Kim Y, Bae J, Kim T G, Kim J W, Lee D C and Jeong S 2017 *Chem. Mater.* **29** 7088